

An Estimate of Solar Wind Density and Velocity Profiles in a Coronal Hole and a Coronal Streamer

M. Pätzold

Institut für Geophysik und Meteorologie, Universität zu Köln, Germany

H. Tsurutani

Jet Propulsion Laboratory, California Institute of Technology, Pasadena, USA

M.K. Bird

Radioastronomisches Institut, Universität Bonn, Germany

Short title: CORONAL DENSITY AND VELOCITY PROFILES

Abstract. Using the total electron content data obtained by the Ulysses Solar Corona Experiment (SCE) during the first solar conjunction in summer 1991, two data sets were selected, one associated with a coronal hole and the other associated with coronal streamer crossings. In order to determine coronal streamer density profiles, the electron content of the tracking passes embedded in a coronal streamer were corrected for the contributions from coronal hole densities. The inferred streamer electron density profile has a radial fall-off exponent of -2.4 for distances greater than 7 solar radii implying the acceleration of the slow solar wind according to $v(r) \sim r^{0.4}$. The acceleration terminates beyond 60 solar radii in agreement with Helios *in situ* observations. All radial electron density profiles inferred from coronal radio sounding observations, particularly during times of high solar activity, are dominated by coronal streamer contributions. They are applicable to coronal streamers, confined to a limited latitude range about the heliospheric current sheet and they are *not* representative of a large scale mean coronal electron density profile. A similar analysis of the coronal hole electron content data was not unequivocally feasible due to a lack of data. The coronal hole tracking passes corrected for contributions from coronal streamer areas display large electron content and density fluctuations. Assuming that the lowest densities represent typical hole densities and comparing these with streamer densities at the same distance, the streamer-to-hole density ratio is found to be a factor of ten, which agrees with white-light coronagraph results.

Introduction

The Ulysses Solar Corona Experiment (SCE) was performed during the first solar conjunction of the Ulysses spacecraft from 1991 May to September. The corona was sounded for distances of the proximate point of the radio ray path from about 4-40 solar radii (R_{\odot}) on both sides of the solar limb. A detailed description of SCE may be found in Bird et al. (1992), the results of the dual-frequency ranging observations in Pätzold et al. (1992) and Bird et al. (1994).

The goal of this study is the determination of the electron density and acceleration profile of the solar wind in the inner corona inside an equatorial coronal hole and the streamer belt. Densities of the inner solar corona were inferred from white light coronagraph observations inside $5 R_{\odot}$ (e.g., Skylab: Munro & Jackson, 1977; Guhathakurta & Holzer, 1994; Guhathakurta et al., 1996; Spartan 201: Guhathakurta & Fisher, 1995; Fisher & Guhathakurta, 1995). The closest *in situ* observations of the density in the inner heliosphere were made with Helios outside $60 R_{\odot}$. Sounding the solar corona with spacecraft radio signals during superior solar conjunction is one of the few techniques used to close the gap between the white light and the *in situ* observations (e.g., Tyler et al., 1977; Muhleman & Anderson, 1981; Anderson et al., 1987; Krisher et al., 1991; Bird et al., 1994; Pätzold et al., 1995). A solar wind speed profile was derived from electron densities determined during the Viking solar conjunction (Muhleman & Anderson, 1981) without distinction between coronal holes and streamers. Spectral broadening was used to derive speeds at $1.7 R_{\odot}$ (Woo, 1978) and flow speeds of a CME (Woo & Armstrong, 1981). Two-station correlations of scintillating spacecraft signals have provided additional velocity estimates at these intermediate solar distances (e.g., Armstrong & Woo, 1981).

Observations of the interplanetary scintillation (IPS) of compact natural radio sources can also be used to estimate the solar wind velocity (Armstrong et al., 1986; Grail et al., 1996). The source signal is scattered by electron density irregularities moving with the solar wind so that the signal intensity varies with time and position at the Earth (e.g., Armstrong and Coles, 1972; Coles and Kaufman, 1978; Armstrong et al., 1986; Grail et al., 1996). IPS

latitudinal coverage is better, because there are many sources at various elongations to the ecliptic. latitudinal coverage using occulted spacecraft signals depends on the spacecraft's interplanetary orbit. Significant latitudinal dependencies in spacecraft coronal sounding data were observed with Viking (Tyler et al., 1977; Muhleman and Anderson, 1981) and during the second Ulysses conjunction in February/March 1995 (Pätzold et al., 1995; Bird et al., 1996).

Coronal Sounding Observations

The nominal SCE radio system configuration was to transmit two downlinks at S-band (2.3 GHz) and X-band (8.4 GHz), both of which were phase coherent with the S-band uplink at 2.1 GHz. The “observable” is the differential group delay time $\Delta\tau$, the delay of the S-band ranging code relative to the X-band code. This differential group delay time is directly proportional to the total electron content N_T , the integrated electron density along the ray path (e.g., Bird et al., 1994):

$$\Delta\tau = \frac{40.31}{c} \left[\frac{1}{f_S^2} - \frac{1}{f_X^2} \right] \quad (1)$$

where c is the speed of light and f_S and f_X are the S-band and X-band carrier frequencies, respectively. The total electron content is defined as:

$$N_T = \int_0^s N(r) ds \quad (2)$$

with $N(r)$ the electron density along the ray path at the distance r from the Sun and s is the length of the ray path from spacecraft to the Earth (see Figure 1)

Figure 1

To a rough approximation, the electron density distribution is often taken to be spherically symmetric and depending on radial distance according to the inverse square law:

$$N(r) = N_0 \cdot \left[\frac{R_0}{r} \right]^2 \quad (3)$$

with N_0 the electron density at R_0 (see also Fig. 1). in this case the integral (2) is simply given by:

$$N_T = N_0 \cdot \frac{R_0^2}{R} \cdot \int_0^{ESU} d\beta = N_0 \cdot \frac{R_0^2}{R} \cdot ESU \quad (4)$$

where $R = u \cdot \sin(SUE)$ is the closest approach distance of the radio ray path to the Sun (solar offset). From (4), it is clear that $N_T \sim R^{-1}$.

The electron density, however, may deviate slightly from the r^{-2} law according to:

$$N(r) = N_0 \cdot \left[\frac{R_0}{r} \right]^{2+\gamma} \quad (5)$$

which results in:

$$N_T = N_0 \cdot \frac{R_0^{2+\gamma}}{R^{1+\gamma}} \cdot \int_0^{SUE} \sin^\gamma(SUE + \beta) d\beta \quad (6)$$

In this case the total electron content $N_T \sim R^{-1}$ and this seems to be supported by many coronal sounding observations (e.g., Muhleman & Anderson, 1981; Anderson et al., 1987; Krisher et al., 1991; Pätzold et al., 1992; Bird et al., 1994). However, a basic assumption in all these cases is a spherically symmetric electron density distribution according to (5) along the *entire* ray path from the spacecraft to the Earth.

The inferred total electron content as a function of solar offset in the range 4 to 40 R_\odot from the Ulysses 1991 solar conjunction yielded two single power laws with radial fall-off exponents being $\alpha = -1 \rightarrow \gamma = -1.54 \pm 0.05$ and $\alpha = -1.42 \pm 0.05$ for ingress and egress, respectively. Following (6) and (5), the electron density in this distance range should follow a single power law with radial exponents of -2.54 and -2.42 for ingress and egress, respectively (Bird et al., 1994).

Bird et al. (1994) identified the location of the proximate points of the radio ray paths projected onto a source surface map of the Sun. It turned out that these most significant parts of the ray paths were embedded either in magnetic monopolar structures (coronal holes) or in the dense coronal structures of the heliospheric current sheet (streamer belt). The streamer belt crossings could be seen as deviations from the single power law of the total electron content.

Dual-frequency Ranging Data Analysis: A New Approach

A more detailed analysis of the tracking pass projections onto the source surface map and the Mauna Loa white-light synoptic maps reveals that the radio ray path crossed a series of hole/streamer boundaries with their respective low/high densities (Figure 2). The hole and

streamer regions contribute differently by density and distance to the observed total electron content.

Figure 2

Let us define a coronal hole and a coronal streamer tracking pass if the proximate point of the path to the Sun is located in a coronal hole and a coronal streamer, respectively. For this study, two data sets were selected, where the proximate points of the ray paths are associated with a coronal hole or with the vicinity of the heliospheric current sheet (inside $\pm 20^\circ$ relative to the HCS).

The following assumptions were made in this study: (a) the solar wind is bimodal, the fast, and slow wind originate from coronal holes and the streamer belt, respectively, (b) the boundaries between these two solar wind types are sharp and (c) the coronal structures are stationary for the time of the observations which were made over one solar rotation.

Figures 3 and 4 show the general geometries for a coronal streamer and a coronal hole tracking pass, respectively. In both figures the streamer is the shaded region with boundaries b_2 and b_4 or b_5 . Furthermore, it is assumed that the radio ray propagates both through solar wind regions where the solar wind speed is constant (acceleration terminated) and where the solar wind is still accelerated, the density profiles being given by (3) and (5), respectively. The boundary of the solar wind acceleration termination of each stream can be calculated by (see also Fig. 1)

$$b_i = \arcsin \left[\frac{R}{R_i} \right] \quad \text{--- } SIII < \text{ for } b_i < b_R \quad (7)$$

or by

$$b_i = PSU - SIU - \arcsin \left[\frac{R}{R_i} \right] \quad \text{for } b_i > b_R \quad (8)$$

where the index $i = h, s$ stands for the fast (hole) and slow (streamer) solar wind, respectively.

Figure 3

Referring to Fig. 3 as an example, the contributions to the total electron content in a coronal streamer tracking pass are:

Figure 4

- the integrated electron density proportional to r^{-2} along the ray path embedded in the coronal hole from Ulysses to the point R_h along the ray path where the acceleration of the fast stream is terminated (denoted $6I$). The boundary b_1 on the ray path is located at a distance R_h from the Sun, and was determined using (7).

- the integrated electron density along that part of the path embedded in the acceleration region of the fast stream proportional to $r^{-2-\gamma_h}$ (from b_1 to b_2). b_2 also marks the boundary from the hole into the streamer region.
- the integrated electron density along that part of the path embedded in the region of the slow stream proportional to r^{-2} (from b_2 to b_3).
- the integrated electron density along that part of the path embedded in the acceleration region of the slow stream proportional to $r^{-2-\gamma_s}$ (from b_3 to b_4). The boundaries b_3 and b_4 on the ray path are located at a distance R_s from the Sun, and were determined using (7) and (8), respectively.
- the integrated electron density along that part of the path embedded in the region of the slow stream proportional to r^{-2} (from b_4 to b_5). b_5 also marks the boundary from the streamer into the hole region.
- the integrated electron density along that part of the path embedded in the acceleration region of the fast stream proportional to $r^{-2-\gamma_h}$ (from b_5 to b_6). The boundary b_6 on the ray path is located at a distance R_h from the Sun, and was determined using (8).
- the integrated electron density proportional to r^{-2} along the ray path embedded in the coronal hole from b_6 to the Earth.

Using the geometries in Fig. 1, the total electron content is then given by:

$$\begin{aligned}
 N_T = & N_h \frac{R_0^2}{R} \int_0^{b_1} d\beta + \\
 & N_h \frac{R_0^2}{R} \left[\frac{R_h}{R} \right]^{\gamma_h} \cdot \int_{b_1}^{b_2} \sin^{\gamma_h}(SUI + \beta) d\beta + \\
 & N_s \frac{R_0^2}{R} \int_{b_2}^{b_3} d\beta + \\
 & N_s \frac{R_0^2}{R} \left[\frac{R_s}{R} \right]^{\gamma_s} \cdot \int_{b_3}^{b_4} \sin^{\gamma_s}(SUI + \beta) d\beta + \\
 & N_s \frac{R_0^2}{R} \int_{b_4}^{b_5} d\beta +
 \end{aligned}$$

$$N_h \frac{R_0^2}{R} \left[\frac{R_h}{R} \right]^{\gamma_h} \cdot \int_{b_5}^{b_6} \sin^{\gamma_h} (SU E + \beta) d\beta + N_h \frac{R_0^2}{R} \int_{b_6}^{E_{SU}} d\beta \quad (9)$$

where (R_h, R_s) are the heliocentric distances where the acceleration of the fast or slow wind terminates, (γ_h, γ_s) are the deviations of the radial exponents from the r^2 density distribution for the coronal hole and the coronal streamer inside the acceleration region, and (N_h, N_s) are the electron densities at $R_0 = 1$ AU.

This (general but still simple) example describes seven different regions contributing to the observed total electron content. In this study up to four boundaries (streamer/hole/streamer/hole/streamer) with up to eleven different contributing regions were used. If $R > R_h$ ($b_1 > b_2$ or $b_5 > b_6$ in Fig. 3) the radio ray never crosses the acceleration regions of the coronal hole. Furthermore, if $R < R_s$ ($b_2 > b_3$ or $b_4 > b_5$ in Fig. 3), the ray may never cross streamer regions with constant slow wind speed. In these cases some of the regions have zero width and their respective integrals do not contribute in (9).

In order to determine the contribution of the coronal hole density to the total electron content of a specific radio ray path whose proximate point lies inside a coronal hole, the observed total electron content N_7 must be corrected for the contribution(s) of the density not connected to that coronal hole, i.e., that segment of the ray path inside the high density streamer region(s). This was done by first projecting the ray path onto the the Mk3 white light synoptic maps of the High Altitude Observatory for Carrington Rotations 1845 and 1846, overlaying additionally the Stanford Source Surface Map from the Wilcox Solar Observatory, and then determining the Carrington longitudes of the boundaries between the hole and the streamer areas (see Figure 2) which were assumed to be the intersections of the ray path projections and the 100 pB lines in the Mk3 maps.

By assuming initially R_s , the radial exponent γ_s of the electron density in the acceleration region of the slow solar wind stream and a typical electron density of the slow wind N_s at 1 AU, the integrals of the streamer regions can be solved and this estimate is subtracted from the observed total electron content.

The radial dependence of the corrected electron content (now the electron content of

the coronal hole alone), the exponent γ_h and the electron density N_h at 1 AU is fitted for various R_h by using the nonlinear least-squares Marquardt method as described in Bevington & Robinson (1992).

The above procedure is then applied to those tracking passes having the proximate point of the ray path in the coronal streamer regions, taking the results from the coronal hole as first guesses.

This procedure was iterated until a balance was attained. If-consistent values were determined for the following parameters: N_h, γ_h for the coronal hole and N_s, γ_s for the coronal streamer. The distances of acceleration termination R_h and R_s were varied within reasonable ranges to examine their effects on the above fitted parameters. In summary, the electron density distributions are:

$$\begin{aligned} N_h(R) &= N_h \cdot \left[\frac{R_0}{R} \right]^2 & \text{for } R > R_h \\ N_h(R) &= N_h \cdot \frac{R_0^2}{R^2} \left[\frac{R_h}{R} \right]^{\gamma_h} & \text{for } R < R_h \\ N_s(R) &= N_s \cdot \left[\frac{R_0}{R} \right]^2 & \text{for } R > R_s \\ N_s(R) &= N_s \cdot \frac{R_0^2}{R^2} \left[\frac{R_s}{R} \right]^{\gamma_s} & \text{for } R < R_s \end{aligned} \quad (10)$$

Results for the Coronal Streamer

Density Profile Figure 5 shows the total electron content averaged over the entire tracking pass (typically ~ 8 hours duration) from all coronal streamer tracking passes. The error bars do *not* indicate a statistical observational error, but rather a $\pm \sigma$ fluctuation of the electron content during the tracking pass due to the turbulence of the coronal medium. The error in the determination of the propagation delay of the radio signals is in the order of ± 8 ns corresponding to an error in electron content of ± 35 hexems, much smaller than the typical fluctuation of at least, several hundred hexems. The solid points in Fig. 5 are the observed data, the triangles represent the corrected data. It is clear that the low density coronal hole regions do not contribute significantly to the streamer electron content.

Figure G shows one result of the nonlinear least-squares fit for $R_s = 80 R_\odot$. The thick solid line represents the electron density profile according to (5) with $N_s = 10.5 \pm 1.3 \text{ cm}^{-3}$ and

Figure 5

$\gamma = 0.4 \pm 0.2$, corresponding to a radial electron density falloff $\sim r^{-2.4}$ inside $R_s = 80 R_\odot$. The thin solid lines represent the $\pm \sigma$ statistical error from the fit procedure. The density points with error bars were calculated from the corrected electron content of each tracking pass.

Figure 6

Figure 7 shows the results from the nonlinear least squares fit for varying distances R_s . The value of γ_s remained remarkably constant at $\gamma_s = 0.4$ for increasing R_s , but the error decreased significantly from 20070 at $R_s = 40 R_\odot$ to 20% at $R_s = 210 R_\odot$. The density N_s decreases for larger R_s from $N_s = 13.3 \pm 1.6 \text{ cm}^{-3}$ at $R_s = 40 R_\odot$ to $N_s = 7.3 \pm 1.2 \text{ cm}^{-3}$ at $R_s = 210 R_\odot$. Assuming a typical density of 10 cm^{-3} at 1 AU, the termination of the slow wind acceleration should be located between $60 R_\odot$ and $90 R_\odot$. This is in agreement with *Helios in situ* observations (Schwenn et al., 1981).

Figure 7

Inferred velocity profiles Mass flux conservation from the inner corona to 1 AU requires that:

$$v(R) \cdot N(R) \cdot A(R) = v_s \cdot N_s \cdot A_s = \text{constant} \quad (11)$$

where $v(R)$ is the solar wind speed at solar offset distance R , and $N(R)$ varies according to (10). The cross sectional area $A(R)$ of the streamtube varies proportional to R^2 and $v_s \cdot N_s \cdot A_s = \text{const}$ is the mass flux at 1 AU. The divergence of $N(R)$ from the simple r^{-2} law is an indicator of the acceleration of the solar wind. Once the acceleration is terminated (at R_h and R_s for the coronal hole and the coronal streamer, respectively), the electron density varies as r^{-2} and $\gamma = 0$. Using (11) and (10) it follows for the velocity $v(R)$ relative to the final velocity v_s

$$\frac{v(R)}{v_s} = \frac{N_s}{N(R)} \cdot \left[\frac{R_0}{R} \right]^2 = \left[\frac{R}{R_0} \right]^{\gamma_s} \quad (12)$$

The velocity of the slow solar wind stream thus varies as $r^{0.4}$ over the distance range under consideration (Figure 8) out to the distance of acceleration termination R_s .

Figure 8

Results for the Coronal Hole

Unfortunately, the number of coronal hole tracking passes is considerably less than those of the coronal streamer passes (Figure 9). Only four passes close to the Sun between 5 and $8 R_\odot$ and seven passes between 3.5 and $43 R_\odot$, were found to be useful. Repeating the analysis

of the previous section for coronal streamer passes, the solid points in Fig. 9 represent the total electron content measurements averaged over the tracking pass. The triangles denote the electron content corrected for the average coronal streamer contributions. Even if the proximate point of the ray path is located in a coronal hole, the contributions from the coronal streamer regions dominate the total electron content. In order to derive a density profile in a coronal hole, it is absolutely necessary to correct the data for the streamer contributions.

Figure 9

Figure 10 shows the electron density profile (thick solid line) for $R_h = 15 R_\odot$, for which $N_h = 4.3 \pm 2.9 \text{ cm}^{-3}$ and $\gamma_h = 1.944 \pm 0.01$. This corresponds to a radial electron density falloff exponent of -3.9 inside R_h and -2.0 outside R_h . Unfortunately, the data yield large errors in N_h and a decrease in γ_h for an increase of R_h from 10 to $30 R_\odot$ (see Fig. 11). Taking typical values of 3 cm^{-3} for a fast wind density at 1 AU (Phillips et al., 1995), R_h should be in the range $10\text{--}20 R_\odot$. This is in agreement with recent IPS observations of a polar coronal hole indicating the termination of the fast solar wind acceleration at $10 R_\odot$ (Grail et al., 1996).

Figure 1

Figure 1

Discussion

A comparison with the Spartan 201 electron density observations in polar coronal holes (Fisher & Guthartakurta, 1995) shows that the inferred electron densities from this study are too high for coronal hole densities. A close up of the total electron content is shown in Fig. 12. Each ranging point from the coronal hole tracking passes on 100Y 245 to 248 (32 to $43 R_\odot$) is plotted. The total electron content follows a “zig-zag” pattern, which has been interpreted by Woo (1996) as the signatures of coronal plumes similar to those seen in polar coronal holes in white light data (Fisher & Guthartakurta, 1995), but now extending further out into the corona near equatorial latitudes.

Figure 1

Since the distance of the fast wind acceleration termination R_h is surely inside $30 R_\odot$, the radial density profile should vary proportionally to r^{-2} outside R_h and the density N_h at 1 AU can be calculated from the corrected electron content data in the distance range 34 to $44 R_\odot$. These calculated densities are plotted in Fig. 13.

The large-scale variations in the electron content (approximately 500 hexems over 1.5

days) cannot be eliminated by subtracting only an average contribution from the streamer regions. This leads to the relatively large average coronal hole column densities and, consequently, the large variations in N_h shown in Fig. 13. If the low-latitude coronal plume interpretation of Woo (1996) is correct, the densities in these structures are comparable to the densities in coronal streamers. Assuming that the lowest densities in Fig. 10 represent typical hole densities at about $30\text{--}40 R_\odot$ and comparing these densities with the inferred densities in a coronal streamer for the same distance (Figure 6), the streamer-to-hole density ratio is found to be a factor of ten, which is in agreement with the Spartan-201 results (Guhathakurta & Fisher, 1995).

Figure 1

The conclusion drawn from this study is that all electron density profiles inferred from coronal radio sounding, particularly during times of high solar activity, are dominated by coronal streamer contributions. The radial density profiles are thus more applicable to coronal streamers, confined to a limited latitude range about the HCS, and are *not* generally representative of a large-scale mean coronal electron density profile. One notable exception to this was the Ulysses solar conjunction of 1995, when the apparent track of the spacecraft in the plane of the sky crossed all heliographic latitudes over a narrow range of heliocentric distances. For this unique case a definite distinction between coronal holes and coronal streamers could be drawn (Pätzold et al., 1995; Bird et al., 1996).

References

- Anderson, J. D., 'P. P. Krisher, S. E. Borutzki, M. J. Connally, P. E. Eshe, H. B. Hotz, S. Kinslow, E. R. Kursinski, L. B. Light, S. E. Matousek, K. J. Moyd, D. C. Roth, D. N. Sweetnam and A. H. Taylor, Radio range measurements of coronal electron densities at 13 and 3.6 cm wavelengths during the 1985 solar conjunction of Voyager 2, *ApJ* 323, 1,141-1,143, 1987.
- Armstrong, J. W. and W. A. Colts, Analysis of three station interplanetary scintillation, *J. Geophys. Res.* 27, 4602-4610, 1972.
- Armstrong, J. W. and R. Woo, Solar wind motion within 30 $1 \text{ } \mathcal{R}_{\odot}$: Spacecraft radio scintillation observations, *Astron. Astrophys.* 103, 415-421, 1981.
- Armstrong, J. W., W. A. Colts, H. Kojima and B. J. Rickett, Solar wind observations near the Sun, *The Sun and the Heliosphere in Three Dimensions*, R. G. Marsden (Ed.), Reidel Publishing Company, 59-64, 1986.
- Bevington P. R. and Robinson, D. L., *Data Reduction and error analysis for the physical sciences*, McGraw Hill, New York, 1992.
- Bird, M. K., S. W. Asmar, J. J. Brenkle, P. Edenhofer, M. Pätzold and H. Volland, The coronal sounding experiment, *Astrophys. Suppl. Ser.* 92, 425-430, 1992.
- Bird, M. K., H. Volland, M. Pätzold, P. Edenhofer, S. W. Asmar, and J. J. Brenkle, The coronal electron distribution determined from dual frequency ranging measurements during the 1991 solar conjunction of the Ulysses spacecraft, *Astrophys. J.* 426, 373-381, 1994.
- Bird, M. K., M. Pätzold, P. Edenhofer, S. W. Asmar and 'P. P. McElrath, Coronal radio sounding with Ulysses: Solar wind electron density near 0.1 AU during the 1995 conjunction, *Astron. Astrophys.*, in press, 1996.
- Coles, W. A. and J. J. Kaufman, Solar wind velocity estimation from multi-station 11'S, *Radio Sci.* 13, 591-597, 1978.
- Fisher, R. and M. Guhathakurta, Physical properties of polar coronal rays and holes as observed with the SPARTAN 201-01 coronagraph, *ApJ* 447, 1,139-1,142, 1995.
- Grall, R. R., W. A. Colts, M. T. Klinglesmith, A. It. Breen, P. J. S. Williams, J. Maarkkanen, and R. Esser, Rapid acceleration of the polar solar wind, *Nature* 379, 429-432, 1996.

- Guhathakurta, M. and T.E. Holzer, Density structure inside a polar coronal hole, *ApJ* 426, 782-786, 1994.
- Guhathakurta, M. and R.R. Fisher, Coronal streamers and fine scale structures of the low latitude corona as detected with Spartan 201-01 white light coronagraph, *Geophys. Res. Lett.* 22, 1841-1844, 1995.
- Guhathakurta, M., T.E. Holzer and R.M. MacQueen, The large scale density structure of the solar corona, and the heliospheric current sheet, *Astrophys. J.* 458, 817-831, 1996.
- Krisher, 'J.'., J.D. Anderson, D.D. Morabito, S.W. Asmar, S.F. Borutski, M.J. Delitzki, A.C. Densmore, P.M. Eshe, G.D. Lewis, M.J. Maurer, D.C. Roth, Y.H. So, T.R. Spilker, D.N. Sweetnam, A.H. Taylor, G.J. Tyler, D.J. Gresh and P.A. Rosen, Radio range measurements of coronal electron densities at 13 and 3.6 centimeter wavelengths during the 1988 solar conjunction of Voyager 2, *ApJ* 375, 157-160, 1991.
- Muhleman, D.O. and J.D. Anderson, Solar wind electron densities from Viking dual-frequency radio measurements, *Astrophys. J.* 247, 1093-1101, 1981.
- Munro, R.H. and Jackson, B.V., Physical properties of a polar coronal hole from 2 to 5 solar radii, *Astrophys. J.* 213, 871-886, 1977.
- Pätzold, M., M.K. Bird, H. Volland, P. Edenhofer, S.W. Asmar and J.J. Brenkle, Coronal sounding with Ulysses: Preliminary results from the first solar conjunction, *Solar Wind Seven*, Eds. E. Marsch and R. Schwenn, Pergamon Press, 237-240, 1992.
- Pätzold M., M.K. Bird, P. Edenhofer, S.W. Asmar, and T.P. McElrath, Dual-frequency radio sounding of the solar corona during the 1995 conjunction of the Ulysses spacecraft, *Geophys. Res. Lett.* 22, 3313-3316, 1995.
- Pätzold, M., J. Karl and M.K. Bird, Coronal radio sounding with Ulysses: dual-frequency phase scintillation spectra in coronal holes and streamers, *Astron. Astrophys.*, in press, 1996.
- Phillips, J.J., S.J. Bame, W.C. Feldman, B.F. Goldstein, J.T. Gosling, C.M. Hammond, D.J. McComas, M. Neugebauer, E.F. Scime and S.T. Suess, Ulysses solar wind plasma observations at high southerly latitudes, *Science* 268, 1030-1033, 1995.
- Schwenn, R., K.-H. Mühlhäuser, E. Marsch, and H. Rosenbauer, Two states of the solar wind

- at the time of solare activity minimum, 11. Radial gradients of plasma parameters in fast and slow streams, *Solar Wind Four*, II. Rosenbauer (Ed.), 126-130, 1981.
- Tyler, G.L., J.P. Brenkle, T.A. Komarek, and A.J. Zygielbaum, The Viking solar corona experiment, *J. Geophys. Res.* 82, 4335-4340, 1977.
- Woo, R., Radial dependence of solar wind properties deduced from Helios 1/2 and Pioneer 10/11 scattering observations, *ApJ* 219, 727-739, 1978.
- Woo, R. and J.W. Armstrong, Measurements of a solar flare-generated shock wave at $13.1 R_{\odot}$, *Nature* 292, 608-610, 1981.
- Woo, R., J.W. Armstrong, M.K. Bird and M. Pätzold, Variation of fractional electron density fluctuations inside $40 R_{\odot}$ observed by Ulysses ranging measurements, *Geophys. Res. Lett.* 22, 329-332, 1995.
- Woo, R., Detection of low-latitude plumes in the outer corona by Ulysses radio ranging measurements, *Astrophys. J.* 464, 195-198, 1996.

Martin Pätzold, Institut für Geophysik und Meteorologie, Universität zu Köln, Albertus-Magnus-Platz, 1-50923 Köln, Germany

Bruce T. Tsurutani, Jet Propulsion Laboratory, California Institute of Technology, 4800 Oak Grove Drive, Pasadena, CA 91109, USA

Michael K. Bird, Radioastronomisches Institut, Universität Bonn, Auf dem Hügel 71, 1-53121 Bonn, Germany

Received 01.01.2000; revised 01.01.2000; accepted 01.01.2000.

Acknowledgments. The source surface map data were provided by Todd Hoeksema, Wilcox Solar Observatory, Stanford University. The white light synoptic maps were provided by the Mauna Loa High Altitude Observatory, Boulder, Colorado. The SCL observations were made with the radio antennas of the NASA Deep Space Network with support of

With the extension package 'AGU++', version 1.2 from 1995/01/12

the Multimission Radio Science Support- Team at the Jet Propulsion laboratory, Caltech, Pasadena, headed by Sami W. Asmar. This work was supported by the Deutsche Agentur für Raumfahrtangelegenheiten (DARA) under grants 50 ON 9104 and 50 ON 940]. The responsibility for the contents of this publication is assumed by the authors. Portions of this paper were made at the Jet Propulsion laboratory, California Institute of Technology, under a contract with NASA.

Figure Captions

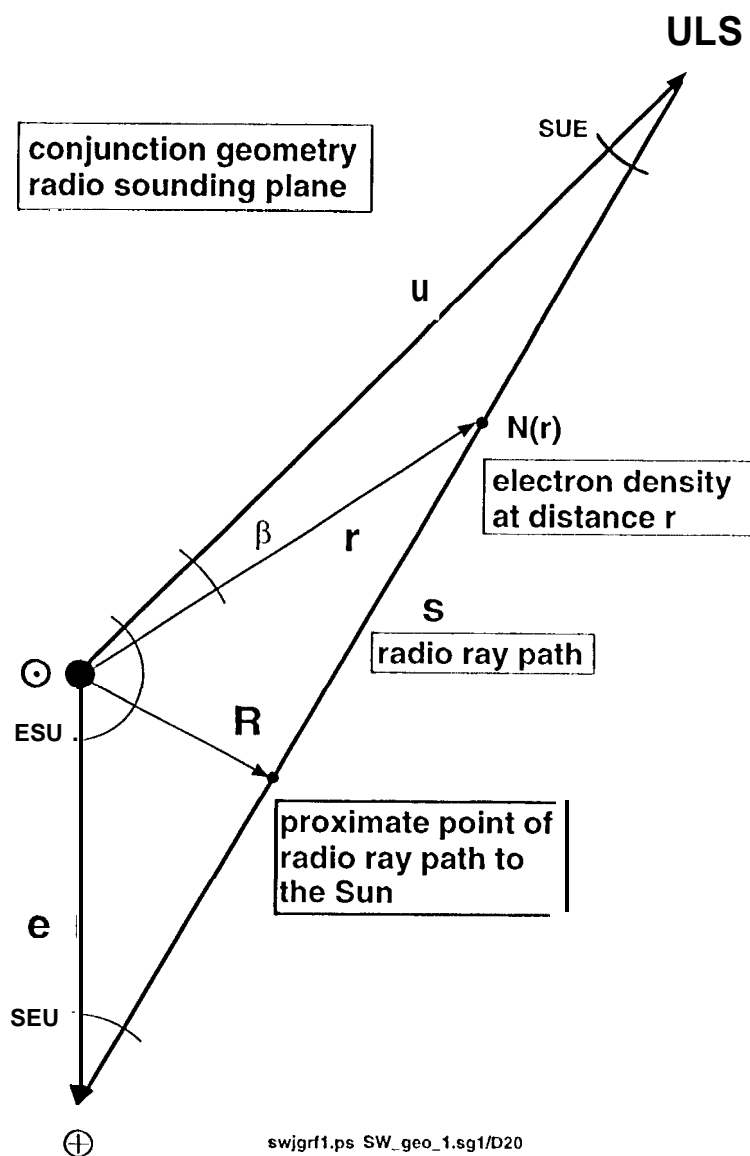


Figure 1. Conjunction geometry for coronal radio sounding. The two heliocentric radius vectors \vec{e} (Sun-Earth) and \vec{u} (Sun-Ulysses) and the radio ray path \vec{s} from Ulysses (ULS) to the Earth (⊕) lie in the so-called radio sounding plane, which does not necessarily coincide with the ecliptic plane or the solar equator. The vector \vec{R} is the radius vector to the proximate point of the radio ray path to the Sun. $N(r)$ is the electron density along the ray path at a distance r from the Sun. The angle between this vector \vec{r} and the vector \vec{u} is β .

CR 1846

CR 1845

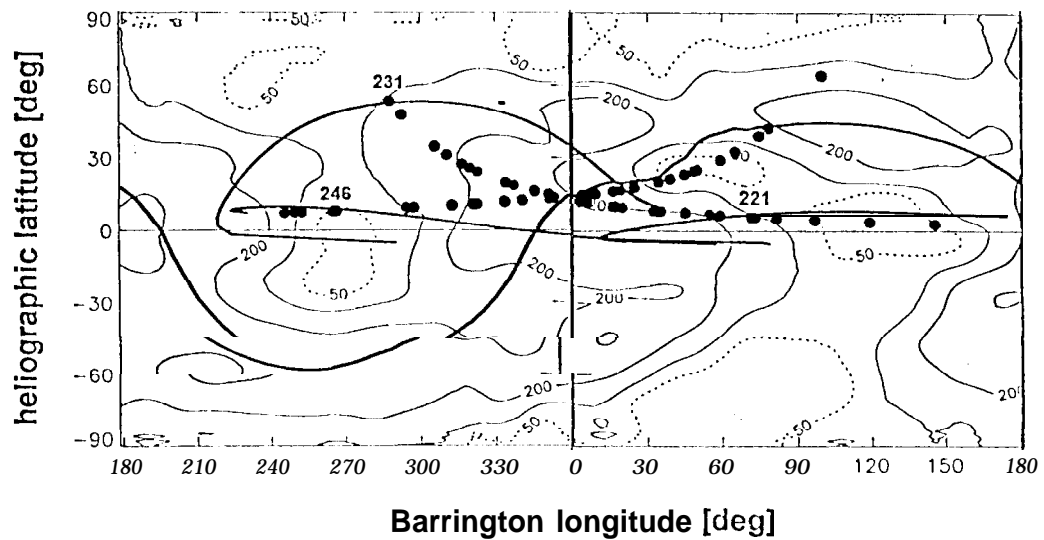


Figure 2. Contour plot of the polarized brightness (pB) in white light using synoptic observations from the Mk3 coronagraph of the High Altitude Observatory on Mauna Loa, Hawaii, for Barrington rotations 1845 and 1846. Overlaid is the trace of the heliospheric current sheet (thick solid line), as inferred from potential field calculations (source surface maps) using synoptic observations from the Wilcox Solar Observatory. Some examples of radio ray paths from Ulysses to the Earth are projected on these maps.

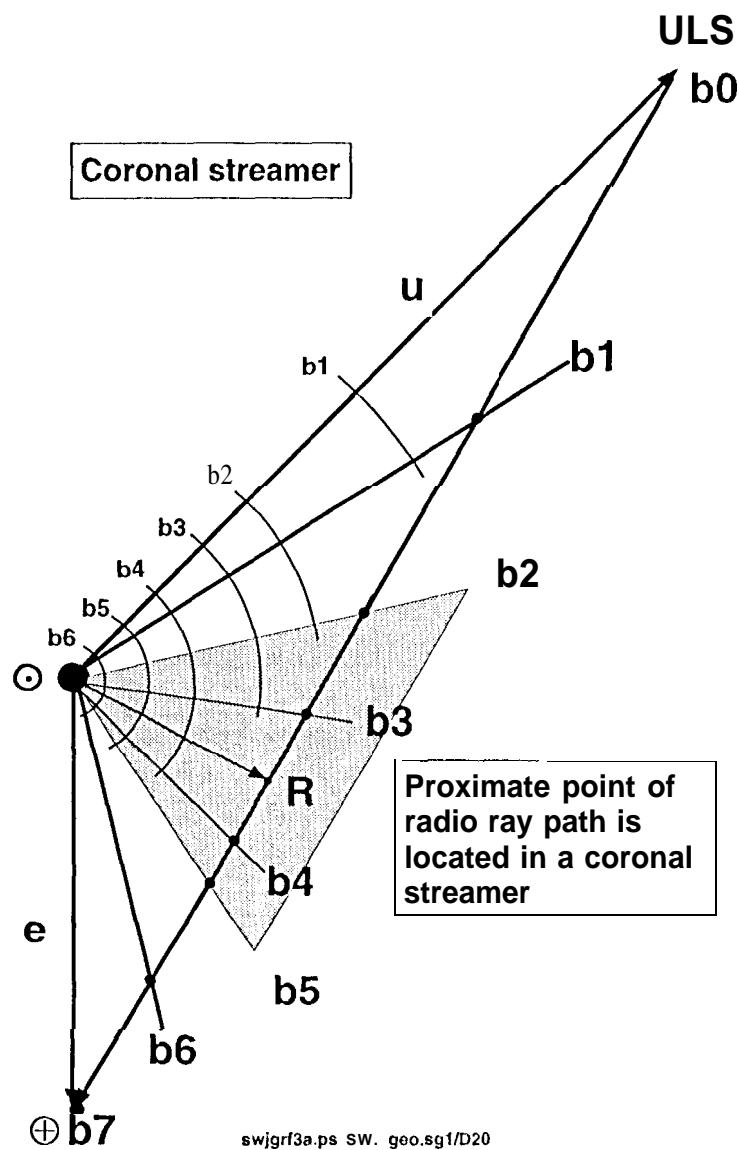


Figure 3. Conjunction geometry of a coronal streamer tracking pass. The proximate point of the radio ray path R is located in a coronal streamer (gray area) with hole/streamer and streamer/hole boundary angles b_2 and b_5 , respectively. The positions of Ulysses (U) and the Earth (\oplus) are located in a coronal hole. The boundary angles b_1 , b_6 and b_3 , b_4 reflect the positions on the ray path where the solar wind acceleration of the fast wind and the slow wind, respectively, is terminated.

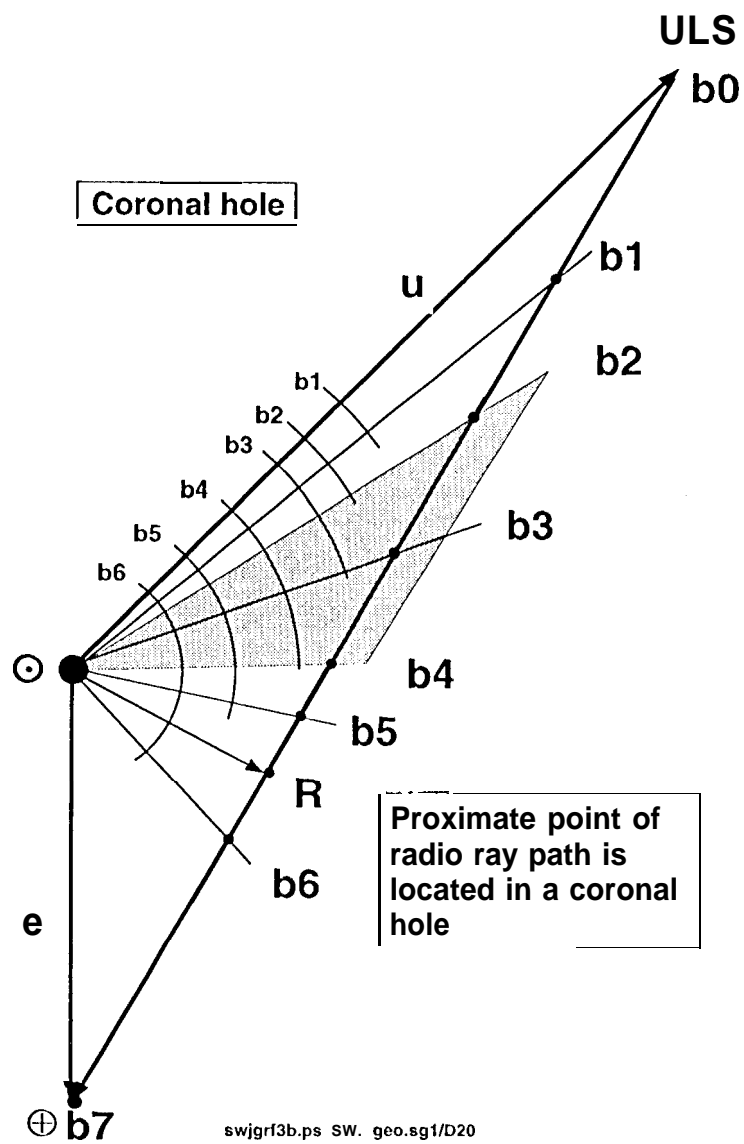


Figure 4. Conjunction geometry of a coronal hole tracking pass with the proximate point of the ray path R located in a coronal hole.

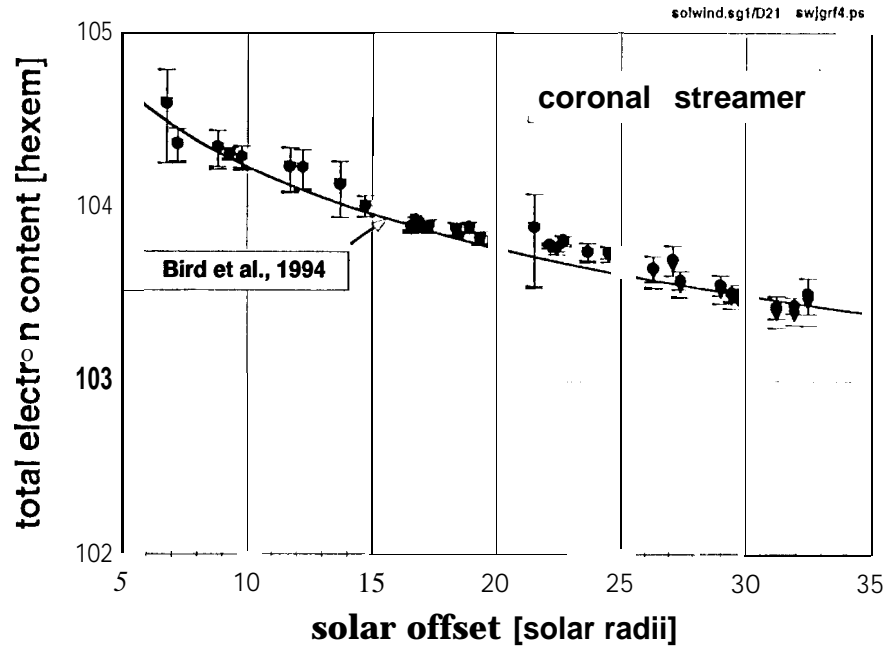


Figure 5. Total electron content measurements (solid points) in all coronal streamer tracking passes as a function of the closest approach distance of the proximate point of the ray path to the sun. The electron content corrected for the coronal hole contributions along the ray path is represented by triangles. The error bars represent the $\pm\sigma$ fluctuation of the electron content due to the turbulent solar wind medium and does *not* represent a statistical observational error. The single power law dependence of the observed electron content found by Bird et al. (1994) is shown for comparison.

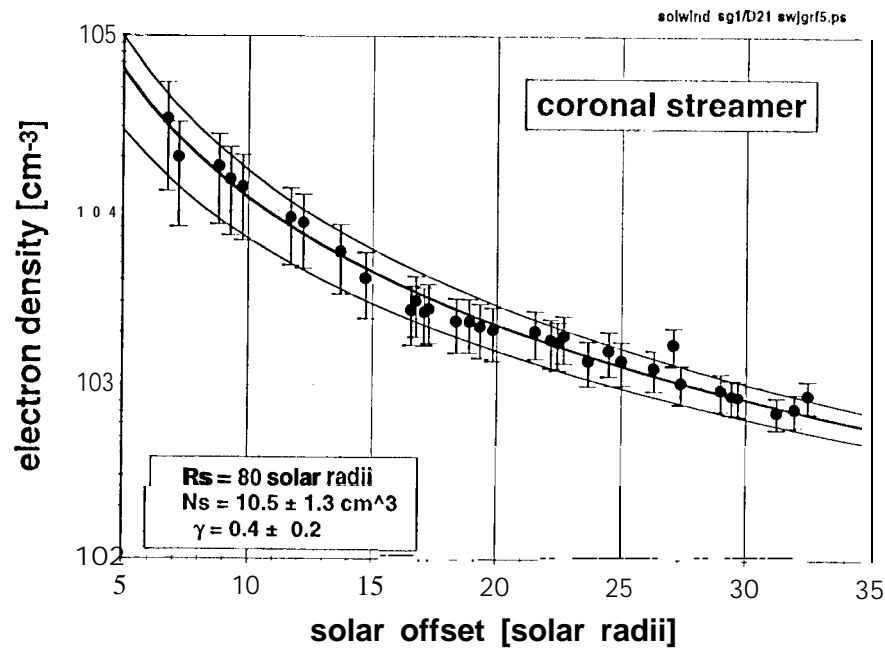


Figure G. Inferred electron densities from the nonlinear least-squares fit for $R_s = 80R_\odot$. The thick solid line is the density profile of the fit parameters $N_s = 10.5 \pm 1.3 \text{ cm}^{-3}$ and $\gamma_s = 0.4 \pm 0.2$. The two thin solid lines are the $\pm\sigma$ error of the profile. A $\gamma_s = 0.4$ corresponds to a radial falloff exponent for the density profile of -2.4 . The points with error bars are the calculated electron densities from the corrected electron content of each tracking pass.

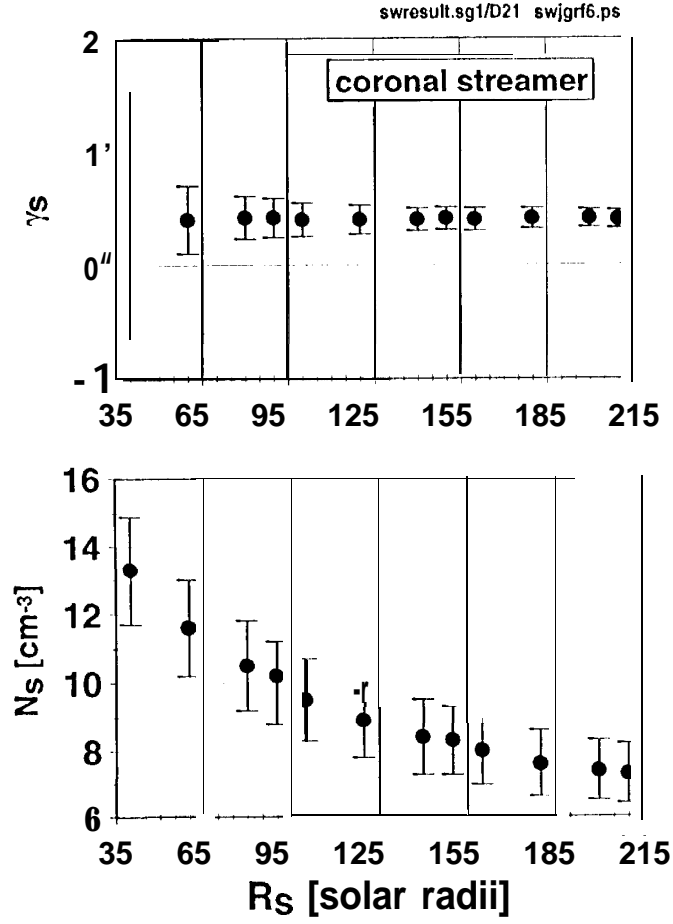


Figure 7. Nonlinear fit results γ_s (upper panel) and N_s (lower panel) for various R_s . Typical density values of 10 cm^{-3} observed at 1 AU in slow solar wind streams suggest a range for R_s between $60 R_\odot$ and $90 R_\odot$.

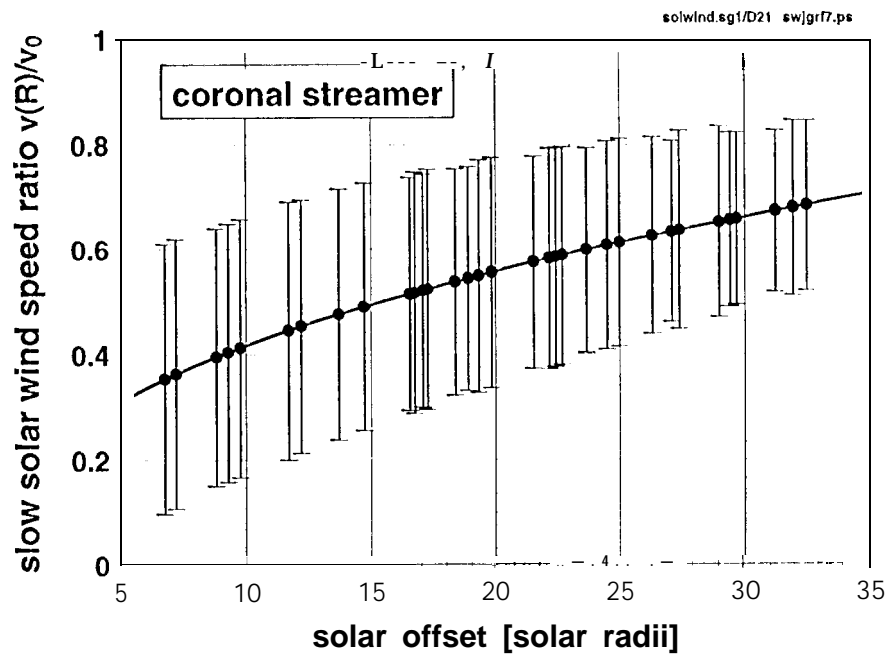


Figure 8. Slow solar wind speed as inferred from the streamer electron density profile assuming mass flux conservation.

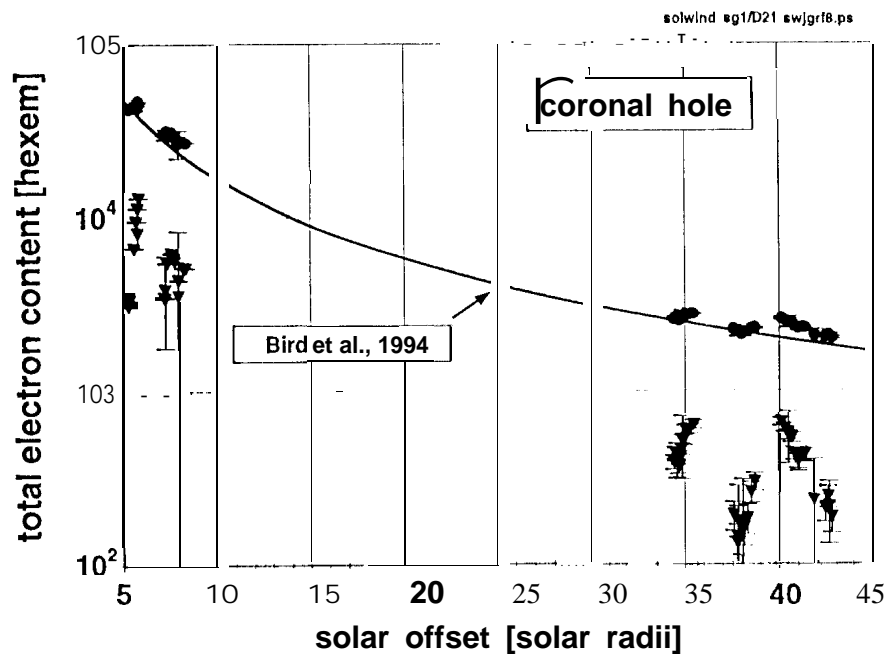


Figure 9. Total electron content measurements in coronal hole tracking passes as a function of the closest approach distance of the proximate point of the ray path to the Sun. Every tenth ranging point of the tracking passes, rather than a value averaged over the tracking pass, is shown as a solid point. The electron content corrected for the coronal hole contributions along the ray path is represented by triangles. The error bars represent the $\pm \sigma$ fluctuation of the electron content due to the turbulent solar wind medium. The single power law dependence of the observed electron content found by Bird et al. (1994) is shown for comparison.

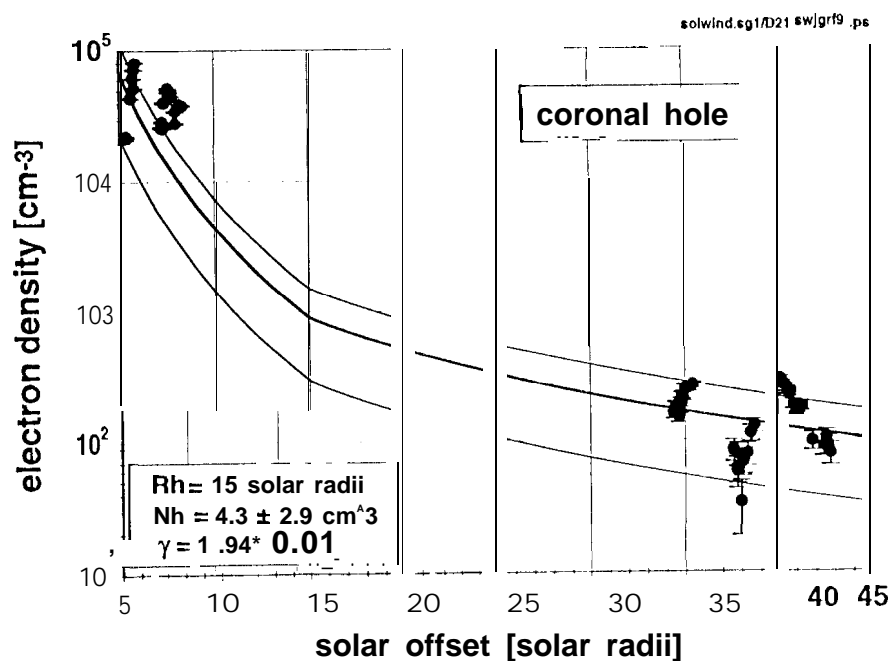


Figure 10. Inferred electron densities from the nonlinear least squares fit for $R_h = 151 \pm 1$. The thick solid line is the density profile of the fit parameters $N_h = 4.3 \pm 2.9 \text{ cm}^{-3}$ and $\gamma_h = 1.94 \pm 0.01$. The two thin solid lines are the $\pm\sigma$ errors of the profile. A $\gamma_h = 1.94$ corresponds to a radial fall-off exponent for the density profile of -3.94 . The points with error bars are the calculated electron densities from the corrected electron content of each tracking pass.

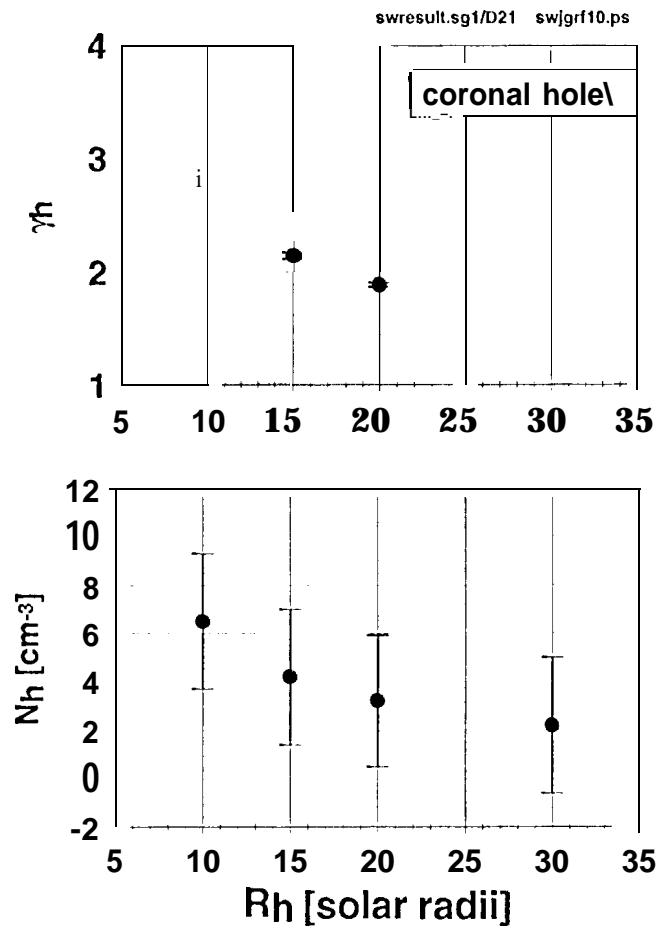


Figure 11, Results from the nonlinear least-squares fit parameters γ_h and N_h in a coronal hole for various R_h .

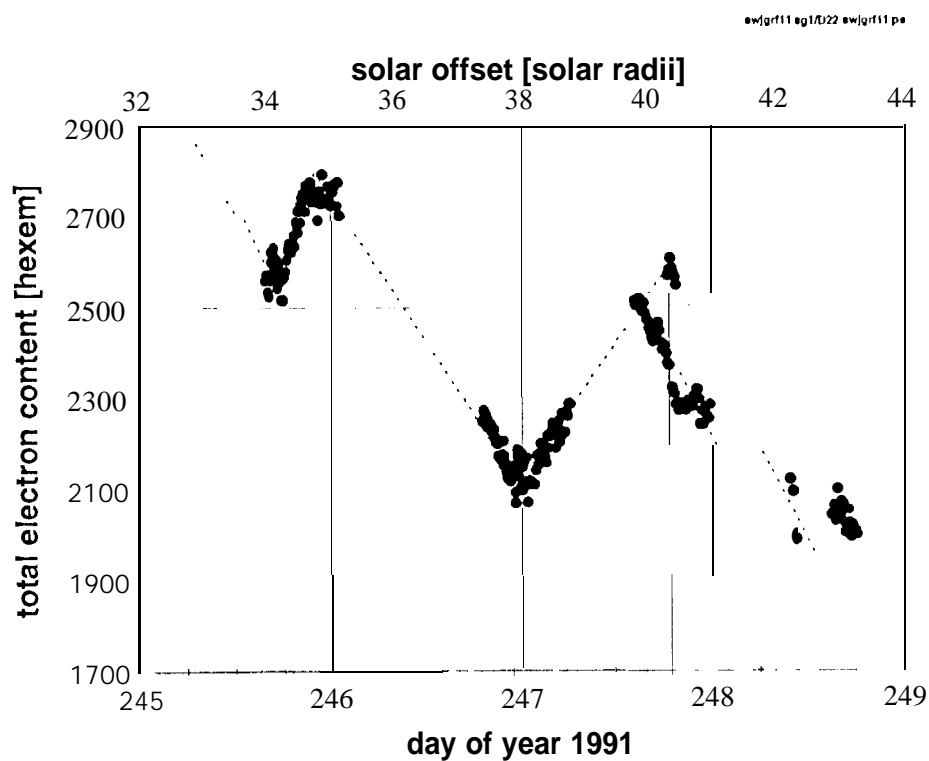


Figure 12. Total electron content measurements on DOY 245 to 248. The data follow a “zig-zag” pattern due either to fluctuations and events in the streamer regions which dominate the contributions to the total electron content or perhaps to low-latitude coronal plumes (Woo, 1996).

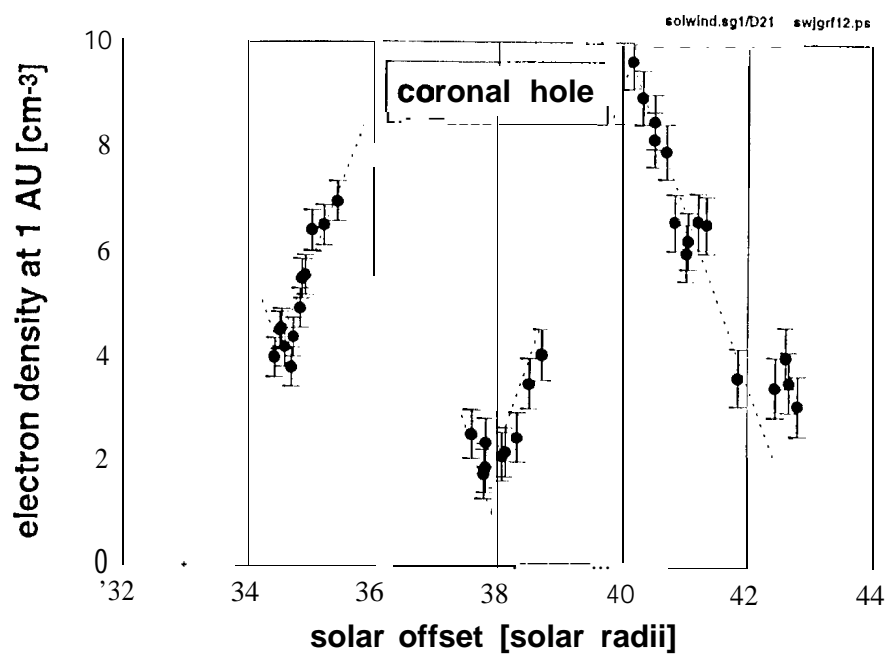


Figure 13. Electron densities at 1 AU calculated from the corrected corona hole electron content data in the distance range 33 to 44 R_{\odot} . The density varies from typical fast wind densities of 3 cm^{-3} to much higher values near 10 cm^{-3} .